ACS APPLIED MATERIALS & INTERFACES

Research Article

www.acsami.org

Ultrathin $Na_{1.1}V_3O_{7.9}$ Nanobelts with Superior Performance as Cathode Materials for Lithium-Ion Batteries

Shuquan Liang,[†,‡] Jiang Zhou,[†] Guozhao Fang,[†] Jing Liu,[†] Yan Tang,[†,‡] Xilin Li,[†] and Anqiang Pan*[,†,‡]

[†]School of Material Science and Engineering, Central South University, Changsha 410083, Hunan, China

[‡]Key Laboratory of Nonferrous Metal Materials Science and Engineering, Ministry of Education, Central South University, Changsha 410083, Hunan, China

Supporting Information

ABSTRACT: The $Na_{1.1}V_3O_{7.9}$ nanobelts have been synthesized by a facile and scalable hydrothermal reaction with subsequent calcinations. The morphologies and the crystallinity of the nanobelts are largely determined by the calcination temperatures. Ultrathin nanobelts with a thickness around 20 nm can be obtained, and the TEM reveals that the nanobelts are composed of many stacked thinner belts. When evaluated as a cathode material for lithium batteries, the $Na_{1.1}V_3O_{7.9}$ nanobelts exhibit high specific capacity, good rate capability, and superior long-term cyclic stability. A high specific capacity of 204 mA h g^{-1} can be delivered at the current density of 100 mA g^{-1}. It shows excellent capacity retention of 95% after 200 cycles at the current density of 1500 mA g^{-1}. As demonstrated by the ex situ XRD results, the $Na_{1.1}V_3O_{7.9}$ nanobelts have very good structural stability upon cycling. The superior electrochemical performances can be attributed to the ultra-thin nanobelts and the good structural stability of the $Na_{1.1}V_3O_{7.9}$ nanobelts.

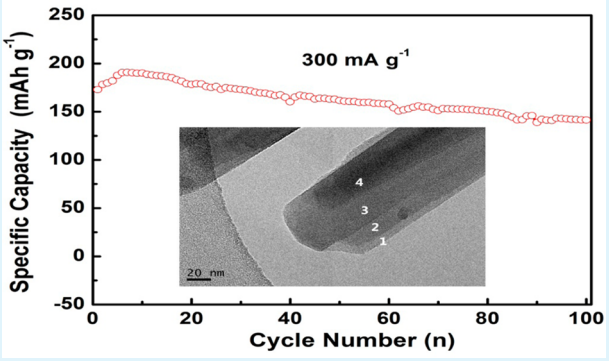

KEYWORDS: *sodium vanadium oxides, nanobelts, structural stability, long-term cyclic stability, lithium ion batteries*

INTRODUCTION

Over the past decades, vanadium-based oxides and vanadates (such as V_2O_5, VO_2, LiV_3O_8, $Ag_2V_4O_{11}$, $AgVO_3$, $Ag_4V_2O_6F_2$, CuV_2O_6, etc.) have been extensively investigated as cathode materials because of their high specific capacity, high energy density, low cost, and abundant resources.[1−13] For example, vanadium pentoxide (V_2O_5) has an ultrahigh theoretical capacity of 442 mA h g^{-1} when three lithium ions are intercalated. LiV_3O_8, with excellent structural reversibility during cycling, can also hold several lithium ions per formula to achieve high theoretical capacity.[14] Transition-metal vanadates also have attracted remarkable attention because of their high specific capacity. Ma et al.[15] report a facile hydrothermal route for the synthesis of CuV_2O_6 nanowires, and it can exhibit a high specific discharge capacity of 514 mA h g^{-1}. As is well-known, vanadium-based oxides and vanadates deliver higher specific capacity than the dominant cathode materials currently used in lithium-ion batteries, such as $LiCoO_2$, $LiMn_2O_4$, and $LiFePO_4$. However, the generally studied vanadium-based oxides and vanadates suffer from the drawbacks of an intrinsic low lithium ion diffusion coefficient, poor electronic conductivity, and inferior long-term cyclic performance.[16] Many transition-metal vanadates are commonly studied as cathode materials for primary lithium batteries due to their large initial capacity but poor cyclic stability.[6] Therefore, considerable efforts have been devoted to improve their long-term cyclic stability.

Recently, sodium vanadium oxides have attracted much attention as cathode materials for lithium ion batteries because of their low cost, high specific capacity, and good rate capability.[17−24] Wang and his co-workers have reported a series of sodium vanadium oxides, showing high rate capability and good cycling stability for rechargeable lithium batteries.[19−21] Nagaraju and Chandrappa[23] have prepared $Na_{0.28}V_2O_5$ nanorings/nanobelts, which exhibit an initial discharge capacity of 320 mA h g^{-1}. Baddour-Hadjean et al.[25] have reported the structural response of β-$Na_{0.33}V_2O_5$ upon Li^+ accommodation in the potential range of 3.8−2.2 V. Liu et al.[17] have reported the synthesis of NaV_6O_{15} nanorods and their good electrochemical behavior as cathode material in rechargeable lithium batteries. However, $Na_{1.1}V_3O_{7.9}$, among the aforementioned sodium vanadium oxides, are much less studied. Recently, Wang et al. have prepared the ultrathin $Na_{1.1}V_3O_{7.9}$ nanosheets with superior rate capability and cycling stability for Li-ion batteries.[19] However, the synthesis process is cumbersome and uniform layer-by-layer stacked nanobelt structure of $Na_{1.1}V_3O_{7.9}$ has not ever been reported.

In this work, we report the synthesis of ultrathin $Na_{1.1}V_3O_{7.9}$ nanobelts composed of many stacked thinner belts by a facile and scalable hydrothermal method with subsequent calcina-

Received: June 18, 2013
Accepted: August 15, 2013
Published: August 15, 2013

   dx.doi.org/10.1021/am402352q | ACS Appl. Mater. Interfaces 2013, 5, 8704−8709

tions. The effect of calcination temperature on the nanobelt morphologies and phase crystallinity is investigated. As a cathode material for the lithium battery, the as-prepared nanobelts exhibit good long-term stability and rate capability. The superior performances can be attributed to the ultrathin nanobelts and the good structural stability upon cycling.

EXPERIMENTAL SECTIONS

Materials Synthesis. All chemicals were of analytical purity and were used as received without further purification. Ammonium metavanadate (NH_4VO_3, ≥99.0%), sodium fluoride (NaF, ≥98%), and hydrogen peroxide (H_2O_2, ≥30%) were used as starting materials. In a typical synthesis, 0.8 g of NH_4VO_3 powder was added into 20 mL of deionized water under magnetic stirring for 20 min, followed by adding 2 mL of H_2O_2 to form a bright-yellow solution. Then, 15 mL of NaF solution (0.152 M) was put into the above solution under vigorous stirring for another 30 min. The obtained mixture solution was transferred to a 50 mL polypropylene-lined autoclave and kept in an electrical oven at 205 °C for 48 h. After cooling down naturally, the bright brownish-red solution was dried at 60 °C to get the solids, which were subsequently calcined in the air at 300 °C, 350 °C, 400 °C, 450 °C, and 500 °C for 4 h. The obtained $Na_{1.1}V_3O_{7.9}$ products are designated as N300, N350, N400, N450, and N500, respectively.

Materials Characterization. The phases of the as-prepared products were studied by X-ray power diffraction (XRD, Rigaku D/max2500 XRD with Cu Kα radiation, λ = 1.54178 Å). The morphologies and sizes of the as-prepared products were characterized by scanning electron microscopy (SEM, FEI Nova NanoSEM 230) and transmission electron microscopy (TEM, JEOL JEM-2100F).

Electrochemical Measurements. The as-prepared products, acetylene black, and polyvinylidene fluoride (PVDF) binder were dispersed in an N-methyl-2-pyrrolidone (NMP) solution in a weight ratio of 70:20:10 to make a slurry, which was coated on aluminum foil and dried in a vacuum oven at 90 °C prior to coin-cell assembly. The Li/$Na_{1.1}V_3O_{7.9}$ coin cells are assembled in a glovebox (Mbraun, Germany) using metallic lithium as an anode, a polypropylene separator, and a 1 M solution of $LiPF_6$ in ethylene carbonate/dimethyl carbonate (EC/DMC) (1:1, v/v) as an electrolyte. The galvanostatic charge/discharge performances of the electrodes were evaluated at room temperature using a Land Battery Tester (Land CT 2001A, Wuhan, China) within the voltage range of 1.5−4 V (vs Li/Li^+). The loading of the $Na_{1.1}V_3O_{7.9}$ cathode material for the coin cell test is about 1−2 mg. Cyclic voltammetry (CV) was tested on an electrochemical workstation (CHI660C, China) at a scan rate of 0.1 mV s^{-1} in the voltage range of 1.5−4.0 V (vs Li/Li^+). The electrochemical impedance spectrometry (EIS) was performed on a ZAHNER-IM6ex electrochemical workstation (ZAHNER Co., Germany) in the frequency range of 100 kHz to 10 mHz on a cell in as-assembled condition.

RESULTS AND DISCUSSION

The temperature-dependent phase evolution of the solids after calcinations was determined by XRD, and the results are shown in Figure 1a. The calcination products exhibit similar XRD diffraction patterns, and most of the diffraction peaks can be indexed to a monoclinic crystalline $Na_{1.1}V_3O_{7.9}$ phase (space group $P2_1/m$, JCPDS card 45-0498). The results are in good agreement with the previous reports.[19] The peak intensity increases with the calcination temperatures, indicating the higher crystallinity. However, the most intensive peaks for the obtained $Na_{1.1}V_3O_{7.9}$ vary with the used annealing temperatures. For example, (400) planes have the highest intensity peak for N300, while the strongest peak for N500 is assigned to the (002) planes. The impurity phase of NaV_6O_{15} (JCPDS card 24-1155) is also detected in the patterns, and it is clearly observed that the content of the impurity phase decreases with the increasing calcination temperature. The $Na_{1.1}V_3O_{7.9}$

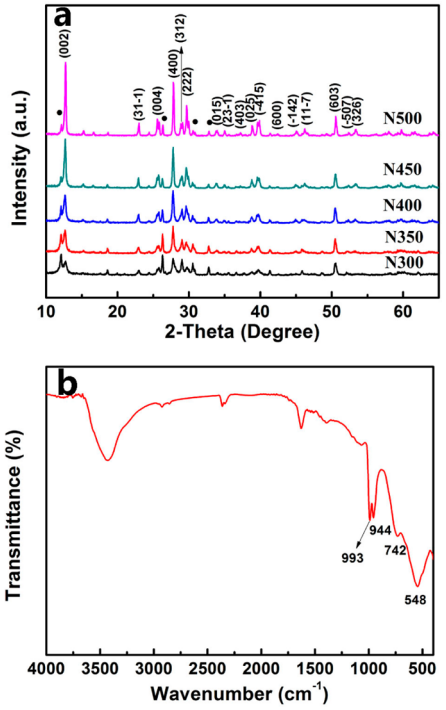

Figure 1. (a) XRD patterns of $Na_{1.1}V_3O_{7.9}$ products synthesized at different temperatures (300 °C, 350 °C, 400 °C, 450 °C, and 500 °C) for 4 h, which are designated as samples N300, N350, N400, N450, and N500, respectively. The weak lines with solid circles are attributed to the impurity phase of NaV_6O_{15}. (b) The FT-IR spectrum of the $Na_{1.1}V_3O_{7.9}$ product synthesized at 300 °C.

nanosheets synthesized by Wang et al. also had the impurity phase of NaV_6O_{15}.[19] The FT-IR spectrum of N300 is shown in Figure 1b. The characteristic absorption peaks are mainly in the range from 400 to 1000 cm^{-1} for the $Na_{1.1}V_3O_{7.9}$ structure. This result is consistent with the previous report, with the V−O stretching vibration observed at 993 and 994 cm^{-1}, and the bands observed at 742 and 548 cm^{-1} can be assigned both to the asymmetric stretching vibrations of V−O−V bonds.[26]

Figure 2 shows the SEM images with different magnifications of the solids synthesized by calcinations at various temperatures from 300 to 500 °C for 4 h. The calcination temperature has an important effect on the morphologies of the final products. As is shown in Figure 2a and b, the product of N300 is composed of a large quantity of nanobelts with a width of 50−500 nm and a length of several micrometers. The thickness of the ultrathin $Na_{1.1}V_3O_{7.9}$ nanobelts is characterized by a higher magnification SEM image (see Figure S1 in the Supporting Information). Ample space can be clearly observed between the nanobelts, and the nanobelts with a smooth surface are very uniform (see Figure 2b). Moreover, the single $Na_{1.1}V_3O_{7.9}$ nanobelt exhibits the interesting layer-by-layer stacked structure (marked in Figure 2b). Figure 2c and d show the SEM image of the N400 sample, which reveals that the nanobelts are getting narrower and thicker. Some particles are of a rod shape. The thickness of the nanobelts is around 56 nm (marked in Figure 2b), which is much thicker than that for N300. When the calcination temperature was raised to 500 °C, the nanobelts completely disappeared and the products (see Figure 2e and f) were typically composed of irregular nanorods, the diameter of which ranged from 200 nm to 1 μm. As is well evidenced by the SEM images, the particles of N500 are much larger and more densely

dx.doi.org/10.1021/am402352q | ACS Appl. Mater. Interfaces 2013, 5, 8704−8709

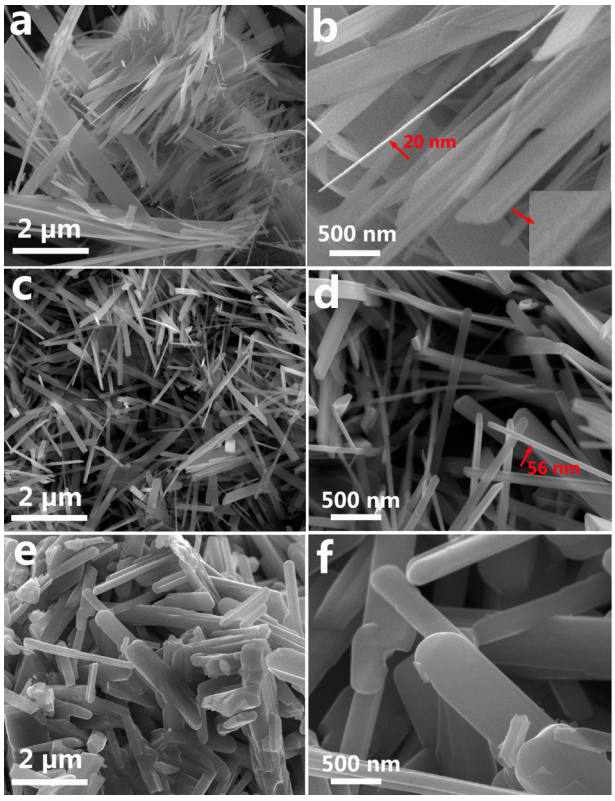

Figure 2. SEM images with different magnifications of $Na_{1.1}V_3O_{7.9}$ products synthesized at different temperatures for 4 h: (a, b) 300 °C, (c, d) 400 °C, (e, f) 500 °C.

packed compared to lower temperature prepared samples, which may be controlled by the kinetics of the phase transition because the formation of larger particles at high temperatures is more kinetically favorable to reduce the surface energy.[27]

Figure 3 shows the TEM images of $Na_{1.1}V_3O_{7.9}$ nanobelts prepared at 300 °C. As shown in Figure 3a, the nanobelts are quite uniform with a typical width of around 100 nm. A higher magnification TEM image (Figure 3b) reveals the layer-by-layer stacking property as indicated by the numbers 1, 2, 3, 4. The thicknesses of the monolayer belts are several nanometers. Recently, Pan et al. prepared the layer-by-layer stacked structure of LiV_3O_8 nanosheets with excellent capacity retention for Li-ion batteries.[14] However, to the best of our knowledge, the layer-by-layer stacked $Na_{1.1}V_3O_{7.9}$ nanobelts have been reported for the first time. A single $Na_{1.1}V_3O_{7.9}$ nanobelt is also characterized by HRTEM, and the result is shown in the inset of Figure 3b. The clear lattice fringes with the interplanar spacings of ~0.209 nm and ~0.215 nm correspond well to the distances of (600) and (60−2) planes of the $Na_{1.1}V_3O_{7.9}$ phase, respectively.

Figure 4a shows the first three successive CV curves of $Na_{1.1}V_3O_{7.9}$ nanobelts prepared at 300 °C. Four strong cathodic

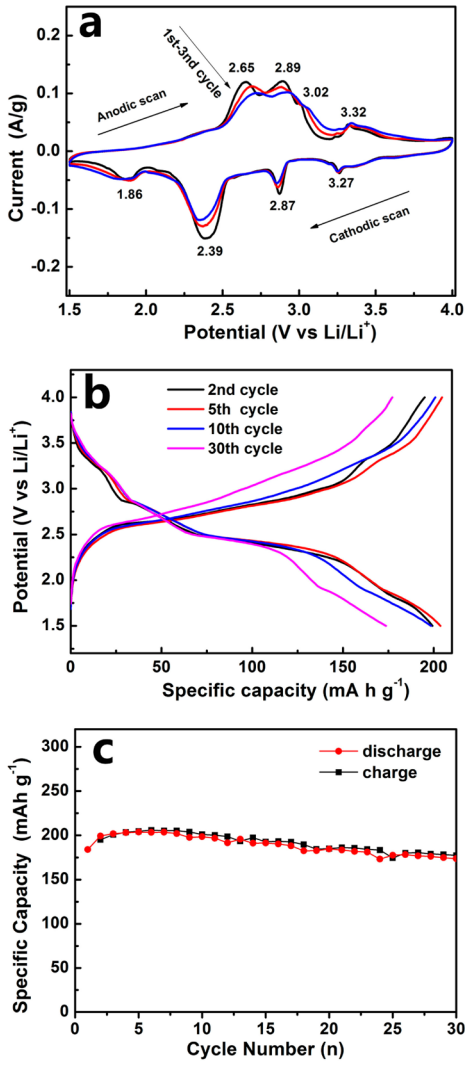

Figure 4. (a) The first three successive CV curves of the N300 electrode at a scan rate of 0.1 mV s^{-1} between 1.5 and 4.0 V. (b) The charge/discharge profiles of the selected cycles and (c) the cycling performances of N300 electrode at the current density of 100 mA g^{-1}.

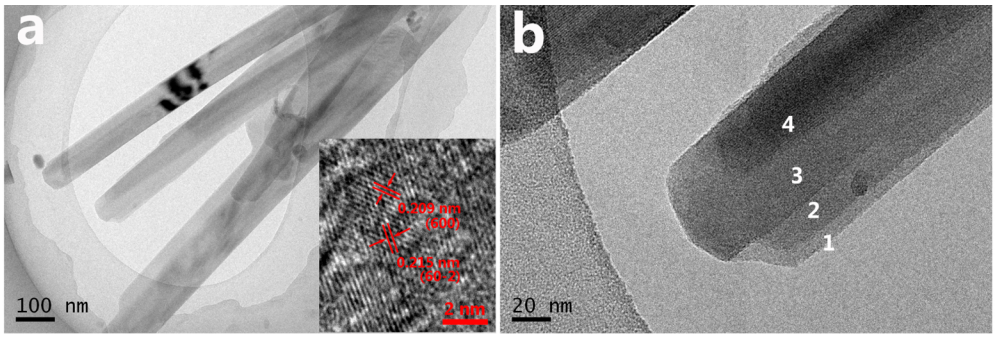

Figure 3. TEM images with different magnifications for $Na_{1.1}V_3O_{7.9}$ nanobelts prepared at 300 °C for 4 h (a, b), and the HRTEM image of $Na_{1.1}V_3O_{7.9}$ nanobelts (inset in a).

dx.doi.org/10.1021/am402352q | ACS Appl. Mater. Interfaces 2013, 5, 8704−8709

peaks at 3.27, 2.87, 2.39, and 1.86 V vs Li/Li^+ are clearly observed, which are related to the Li^+ ion intercalation process. There are also four main anodic peaks appearing at potentials of about 2.65, 2.89, 3.02, and 3.32 V vs Li/Li^+. The results demonstrate the multiple phase transitions during lithium-ion intercalation/deintercalation in the $Na_{1.1}V_3O_{7.9}$ electrode. The cyclic voltammograms are quite similar for the later cycles, which indicate the good reversibility of $Na_{1.1}V_3O_{7.9}$ nanobelts. Figure 4b displays the charge/discharge profiles of the selected cycles for the $Na_{1.1}V_3O_{7.95}$ nanobelts at a current density of 100 mA g^{-1}. Three apparent discharge plateaus are observed at around 1.8, 2.4, and 2.8 V, which are in good agreement with the CV results (shown in Figure 4a). The large overlap of the charge/discharge curves suggests the good structural reversibility of $Na_{1.1}V_3O_{7.9}$ nanobelts. Figure 4c shows the cycling performance of $Na_{1.1}V_3O_{7.9}$ nanobelts at 100 mA g^{-1}. An initial specific discharge capacity of 184 mA h g^{-1} is obtained, and the capacity increases gradually until reaching the maximum value of 204 mA h g^{-1} at the fifth cycle. The $Na_{1.1}V_3O_{7.9}$ nanobelts maintain a specific discharge capacity of 174 mA h g^{-1} after 30 cycles, corresponding to 95% of its initial discharge capacity. The result demonstrates the good cycling stability.

The cycling performances of $Na_{1.1}V_3O_{7.9}$ products are evaluated at the current densities of 300 and 1000 mA g^{-1}, and the results are shown in Figure 5. According to the results,

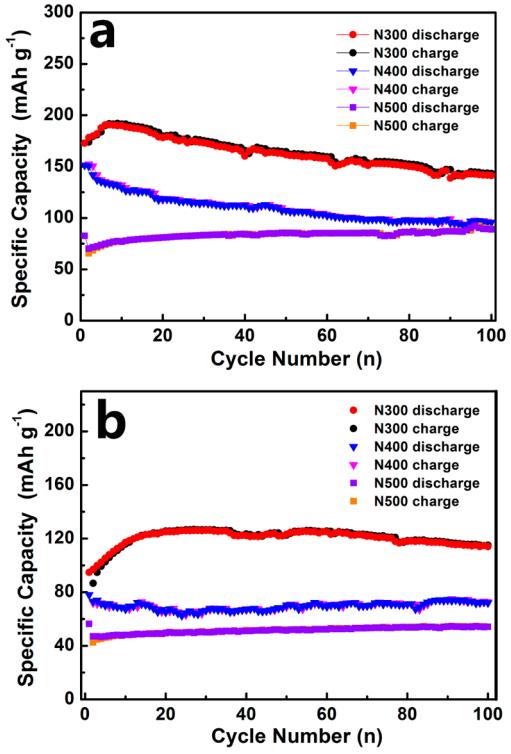

Figure 5. (a, b) Cycling performances of $Na_{1.1}V_3O_{7.9}$ products synthesized at different temperatures at 300 and 1000 mA g^{-1}, respectively.

the $Na_{1.1}V_3O_{7.9}$ nanobelts prepared at 300 °C show the best electrochemical performance at 300 and 1000 mA g^{-1}. A maximum specific discharge capacity of 191 and 126 mA h g^{-1} can be observed for N300 electrode at 300 and 1000 mA g^{-1}, respectively. It delivers an initial discharge capacity of 173 mA h g^{-1} and retains 142 mA h g^{-1} after 100 cycles, which corresponds to 82.1% of its initial discharge capacity with a fading rate of 0.2% per cycle. While the NaV_6O_{15} nanobelt is cycling at a current density of 1000 mA g^{-1}, it still possesses a discharge capacity of 114 mA h g^{-1} after 100 cycles, although a relatively low initial discharge capacity of 95 mA h g^{-1} is detected. However, only a relatively low discharge capacity of 107 and 85 mA h g^{-1} can be obtained after 50 cycles for N400 and N500 at 300 mA g^{-1}, respectively. And they deliver a corresponding discharge capacity of 72 and 54 mA h g^{-1} at a current density of 1000 mA g^{-1} after 50 cycles, respectively. It is worth noting that the $Na_{1.1}V_3O_{7.9}$ nanobelts prepared at 300 °C exhibit the best electrochemical performance. The capacities of N300 at different current densities are increasing with cycling; however, other samples do not show this clear trend. According to the XRD results, the N300 product contains much of the NaV_6O_{15} phase, and recent report showed that the capacities of NaV_6O_{15} material at different current densities exhibit a gradual increasing trend in the initial stage.[17] A possible explanation is that the high content impurity phase of NaV_6O_{15} affects the electrochemical behavior of $Na_{1.1}V_3O_{7.9}$.

In order to understand the good cyclic stability of $Na_{1.1}V_3O_{7.9}$ nanobelts, ex situ XRD probes are used to study the structural changes upon cycling. The XRD patterns of the electrodes before cycling and after 1, 5, 10, and 50 cycles are shown in Figure 6. The principal peaks of $Na_{1.1}V_3O_{7.9}$ are all

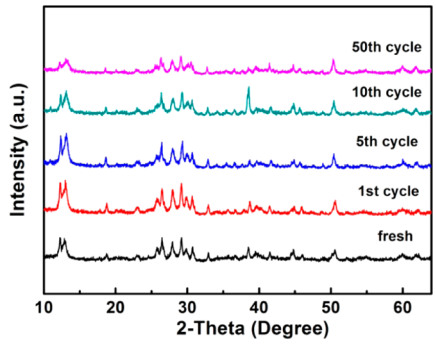

Figure 6. Ex situ XRD patterns of N300 before cycling and after 1, 5, 10, and 50 galvanostatic charge/discharge cycles. The applied current density was 300 mA g^{-1}.

clearly detected for the electrodes before and after cycling, indicating excellent structure stability of $Na_{1.1}V_3O_{7.9}$ nanobelts. The good structural reversibility during cycling can explain the good cyclic stability. The excellent structure stability of $Na_{1.1}V_3O_{7.9}$ during cycling suggests it may be another promising candidate material for rechargeable lithium-ion batteries. According to the ex situ XRD results, the reversible intercalation/deintercalation behavior of Li^+ ions in $Na_{1.1}V_3O_{7.9}$ nanobelts can be expressed as follows:

$$Na_{1.1}V_3O_{7.9} + xLi^+ + xe^- \rightleftharpoons Li_xNa_{1.1}V_3O_{7.9}$$

Figure 7 shows the Nyquist plots of $Na_{1.1}V_3O_{7.9}$ products synthesized at different temperatures. Each Nyquist plot seemed to have a similar shape with a semicircle in the high-frequency region and a straight line in the low-frequency region. The semicircle in the high-frequency region can be associated with the charge-transfer process, which reflects the resistance for Li^+ ion migration through the electrolyte/electrode interface.[28] The inset of Figure 7 shows the equivalent circuit model for the impedance spectra. R_s is the combination of electrolyte resistance and ohmic resistances of cell components. R_f and R_{ct} are represented for the film

dx.doi.org/10.1021/am402352q | ACS Appl. Mater. Interfaces 2013, 5, 8704−8709

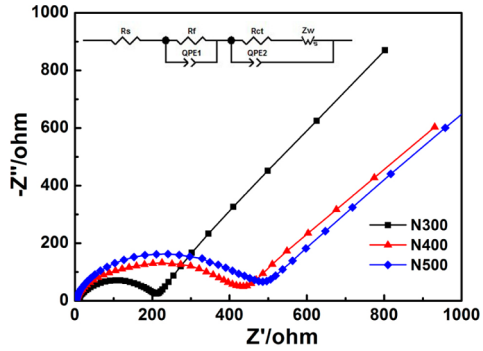

Figure 7. Nyquist plots of $Na_{1.1}V_3O_{7.9}$ products synthesized at different temperatures.

resistance and charge-transfer resistance, respectively. QPE_1, QPE_2, and Z_w are the capacitance of the surface-passivating layer, double layer capacitance, and the Warburg impedance, respectively. Table S1 shows the primary simulation parameters of $Na_{1.1}V_3O_{7.9}$ products. As can be clearly seen in the table, the R_{ct} (charge-transfer resistance) value of N300 (191.5 Ω) is much smaller than those of N400 (273 Ω) and N500 (315 Ω). This can be ascribed to the layer-by-layer ultrathin nanobelt structures of $Na_{1.1}V_3O_{7.9}$, which could reduce the lithium-ion diffusion and electron transportation distance.

Figure 8 shows the long-term cyclic performances of N300. The initial specific discharge capacities of $Na_{1.1}V_3O_{7.9}$ nanobelts

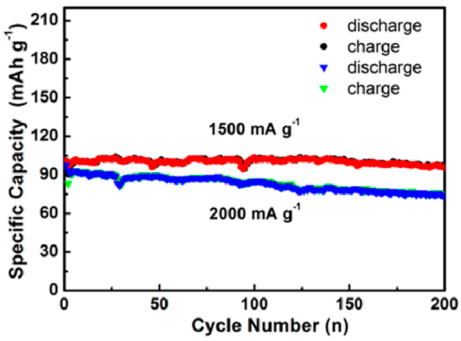

Figure 8. Long-term cycling performances of the N300 electrode under the current densities of 1500 and 2000 mA g^{-1}, respectively.

are 101 and 98 mA h g^{-1} at 1500 and 2000 mA g^{-1}, respectively. After 200 cycles, the $Na_{1.1}V_3O_{7.9}$ nanobelts can still retain a relatively high discharge capacity of 96 mA h g^{-1} at 1500 mA g^{-1}, corresponding to 95% of its initial discharge capacity. A specific discharge capacity of 74 mA h g^{-1} can also be obtained at 2000 mA g^{-1} after 200 cycles with a capacity fading rate of 0.14% per cycle. Both results indicate the superior cyclic stability of the N300 as cathode material for lithium batteries.

The $Na_{1.1}V_3O_{7.9}$ nanobelts exhibit superior electrochemical performance including high specific capacity, high rate capability, and superior long-term cyclic stability when compared to the previous results of vanadium-based oxides and vanadates, such as V_2O_5,[29,30] LiV_3O_8,[31−33] NaV_6O_{15} nanorods,[17] $(NH_4)_{0.5}V_2O_5$ nanobelts,[34] $NH_4V_3O_8{\cdot}0.2H_2O$ flakes,[35] and $Na_2V_6O_{16}{\cdot}xH_2O$ nanowires.[20] The superior electrochemical performances are attributed to the following things: (1) Novel layer-by-layer stacked ultrathin nanobelts: The ultrathin nanobelts shorten the Li^+ ion diffusion and electron transportation distance as well as the enlarged contact area between electrode and electrolyte.[19] (2) Excellent structure stability upon cycling: The good structural reversibility can ensure the repeatable lithium ion intercalation/deintercalation process.

CONCLUSION

In summary, ultrathin $Na_{1.1}V_3O_{7.9}$ nanobelts with superior electrochemical performance have been successfully fabricated using a facile hydrothermal reaction with subsequent calcinations in the air. The as-prepared $Na_{1.1}V_3O_{7.9}$ nanobelts are of the layer-by-layer stacked structures. As a cathode material for lithium batteries, the $Na_{1.1}V_3O_{7.9}$ nanobelts show superior cyclic performance and high rate capability. It is highlighted that the $Na_{1.1}V_3O_{7.9}$ nanobelts have excellent structure stability upon cycling. The superior electrochemical performance suggests their promising applications as a cathode material for rechargeable lithium-ion batteries (LIBs).

ASSOCIATED CONTENT

Supporting Information

The EIS simulation parameters of $Na_{1.1}V_3O_{7.9}$ products and high magnification SEM image of $Na_{1.1}V_3O_{7.9}$ nanobelts. This material is available free of charge via the Internet at http://pubs.acs.org.

AUTHOR INFORMATION

Corresponding Author

*Tel.: (86)-0731-88836069. Fax: (86)-0731-88876692. E-mail: pananqiang@gmail.com.

Notes

The authors declare no competing financial interest.

ACKNOWLEDGMENTS

This work was supported by National High Technology Research and Development Program of China (863 Program) (No. 2013AA110106), Creative Research Group of National Natural Science Foundation of China (Grant No. 50721003), Lie-Ying Program of Central South University and the Fundamental Research Funds for the Central Universities of Central South University (No. 2013zzts181)

REFERENCES

(1) Xu, Y.; Han, X. S.; Zheng, L.; Wei, S. Q.; Xie, Y. *Dalton Trans.* **2011**, *40*, 10751−10757.
(2) Cao, A. M.; Hu, J. S.; Liang, H. P.; Wan, L. J. *Angew. Chem., Int. Ed.* **2005**, *44*, 4391−4395.
(3) Morcrette, M.; Rozier, P.; Dupont, L.; Mugnier, E.; Sannier, L.; Galy, J.; Tarascon, J. M. *Nat. Mater.* **2003**, *2*, 755−761.
(4) Liu, H.; Yang, W. *Energy Environ. Sci.* **2011**, *4*, 4000−4008.
(5) Pan, A.; Liu, J.; Zhang, J.-G.; Cao, G.; Xu, W.; Nie, Z.; Jie, X.; Choi, D.; Arey, B. W.; Wang, C.; Liang, S. *J. Mater. Chem.* **2011**, *21*, 1153−1161.
(6) Cheng, F.; Chen, J. *J. Mater. Chem.* **2011**, *21*, 9841−9848.
(7) Zhao, Q.; Jiao, L.; Peng, W.; Gao, H.; Yang, J.; Wang, Q.; Du, H.; Li, L.; Qi, Z.; Si, Y.; Wang, Y.; Yuan, H. *J. Power Sources* **2012**, *199*, 350−354.
(8) Albrecht, T. A.; Sauvage, F. D. R.; Bodenez, V.; Tarascon, J.-M.; Poeppelmeier, K. R. *Chem. Mater.* **2009**, *21*, 3017−3020.
(9) Xu, X.; Luo, Y.-Z.; Mai, L.-Q.; Zhao, Y.-L.; An, Q.-Y.; Xu, L.; Hu, F.; Zhang, L.; Zhang, Q.-J. *NPG Asia Mater.* **2012**, *4*, e20.
(10) Pan, A.; Wu, H. B.; Yu, L.; Lou, X. W. *Angew. Chem., Int. Ed.* **2013**, *52*, 2226−2230.

(11) Pan, A.; Wu, H. B.; Yu, L.; Zhu, T.; Lou, X. W. *ACS Appl. Mater. Interfaces* **2012**, *4*, 3874−3879.
(12) Bai, L.; Zhu, J.; Zhang, X.; Xie, Y. *J. Mater. Chem.* **2012**, *22*, 16957−16963.
(13) Liang, L.; Zhou, M.; Xie, Y. *Chem. Asian J.* **2012**, *7*, 565−571.
(14) Pan, A.; Zhang, J.-G.; Cao, G.; Liang, S.; Wang, C.; Nie, Z.; Arey, B. W.; Xu, W.; Liu, D.; Xiao, J.; Li, G.; Liu, J. *J. Mater. Chem.* **2011**, *21*, 10077−10084.
(15) Ma, H.; Zhang, S.; Ji, W.; Tao, Z.; Chen, J. *J. Am. Chem. Soc.* **2008**, *130*, 5361−5367.
(16) Pan, A.; Zhang, J.-G.; Nie, Z.; Cao, G.; Arey, B. W.; Li, G.; Liang, S. Q.; Liu, J. *J. Mater. Chem.* **2010**, *20*, 9193−9199.
(17) Liu, H.; Wang, Y.; Li, L.; Wang, K.; Hosono, E.; Zhou, H. *J. Mater. Chem.* **2009**, *19*, 7885−7891.
(18) Nagaraju, G.; Sarkar, S.; Dupont, J.; Sampath, S. *Solid State Ionics* **2012**, *227*, 30−38.
(19) Wang, H.; Liu, S.; Ren, Y.; Wang, W.; Tang, A. *Energy Environ. Sci.* **2012**, *5*, 6173−6179.
(20) Wang, H.; Wang, W.; Ren, Y.; Huang, K.; Liu, S. *J. Power Sources* **2012**, *199*, 263−269.
(21) Zhou, D.; Liu, S.; Wang, H.; Yan, G. *J. Power Sources* **2013**, *227*, 111−117.
(22) Xu, Y.; Han, X.; Zheng, L.; Yan, W.; Xie, Y. *J. Mater. Chem.* **2011**, *21*, 14466−14472.
(23) Nagaraju, G.; Chandrappa, G. T. *Mater. Res. Bull.* **2012**, *47*, 3216−3223.
(24) Lee, C. Y.; Marschilok, A. C.; Subramanian, A.; Takeuchi, K. J.; Takeuchi, E. S. *Phys. Chem. Chem. Phys.* **2011**, *13*, 18047−18054.
(25) Baddour-Hadjean, R.; Bach, S.; Emery, N.; Pereira-Ramos, J. P. *J. Mater. Chem.* **2011**, *21*, 11296−11305.
(26) Subba Reddy, C. V.; Yeo, I.-H.; Mho, S.-i. *J. Phys. Chem. Solids* **2008**, *69*, 1261−1264.
(27) Liang, S.; Zhou, J.; Pan, A.; Zhang, X.; Tang, Y.; Tan, X.; Chen, T.; Wu, R. *J. Power Sources* **2013**, *228*, 178−184.
(28) Yoon, S.; Jo, C.; Noh, S. Y.; Lee, C. W.; Song, J. H.; Lee, J. *Phys. Chem. Chem. Phys.* **2011**, *13*, 11060−11066.
(29) Zhai, T.; Liu, H.; Li, H.; Fang, X.; Liao, M.; Li, L.; Zhou, H.; Koide, Y.; Bando, Y.; Golberg, D. *Adv. Mater.* **2010**, *22*, 2547−2552.
(30) Zhou, X.; Wu, G.; Gao, G.; Cui, C.; Yang, H.; Shen, J.; Zhou, B.; Zhang, Z. *Electrochim. Acta* **2012**, *74*, 32−38.
(31) Feng, Y.; Hou, F.; Li, Y. *J. Power Sources* **2009**, *192*, 708−713.
(32) Liu, Y.; Zhou, X.; Guo, Y. *Electrochim. Acta* **2009**, *54*, 3184−3190.
(33) Sun, J.; Peng, W.; Song, D.; Wang, Q.; Du, H.; Jiao, L.; Si, Y.; Yuan, H. *Mater. Chem. Phys.* **2010**, *124*, 248−251.
(34) Wang, H.; Huang, K.; Huang, C.; Liu, S.; Ren, Y.; Huang, X. *J. Power Sources* **2011**, *196*, 5645−5650.
(35) Wang, H.; Huang, K.; Liu, S.; Huang, C.; Wang, W.; Ren, Y. *J. Power Sources* **2011**, *196*, 788−792.